State Space-Vector Model of Linear Induction Motors

Marcello Pucci, *Senior Member, IEEE*

***Abstract*—This paper presents the state space-vector dynamic model of the linear induction motor (LIM) taking into consideration the dynamic end effects. Starting from the space-vector equivalent circuit of the LIM, the complete set of space-vector equations has been deduced. Afterward, first the so-called voltage and current flux models have been written, from which the complete state space-vector representation has been given. The complete thrust expression including the end-effect braking force has also been introduced in the model. The complete state space-vector model, electromagnetic and mechanical part, has been implemented in numerical simulation and has been validated by comparing the results with those obtainable with a finite-element analysis and experiments. Results show that, even with a machine with a limited presence of the dynamic end effects, the adoption of a this model permits a better estimation of both the electric quantities, e.g., inductor current, and the mechanical quantities, e.g., linear speed, with respect to the classic rotating induction motor model.**

***Index Terms*—End effects, linear induction motor (LIM), space vector, state model.**

NOMENCLATURE

$\mathbf{u}_s$	$u_{sD} + j\ u_{sQ}$. Inductor voltage space vector in the inductor reference frame.
$\mathbf{i}_s$	$i_{sD} + j\ i_{sQ}$. Inductor current space vector in the inductor reference frame.
$\mathbf{i}'_r$	$i_{rd} + j\ i_{rq}$. Induced-part current space vector in the inductor reference frame.
$\boldsymbol{\psi}_\mathbf{s}$	$\psi_{sD} + j\ \psi_{sQ}$. Inductor flux space vector in the inductor reference frame.
$\boldsymbol{\psi}'_r$	$\psi_{rd} + j\ \psi_{rq}$. Induced-part flux space vector in the inductor reference frame.
L_s, L_r, L_m	Inductor, induced-part, and three-phase magnetizing inductances.
$L_{\sigma s}$, $L_{\sigma r}$	Inductor and induced-part leakage inductances.
R_s, R_r	Inductor and induced-part resistances.
p	Number of pole pairs.
ω_r	Angular rotor speed (in electrical angles per second).
v	Linear speed.
τ_m	Length of the inductor.
τ_p	Polar pitch.

Manuscript received November 26, 2012; revised March 5, 2013; accepted March 27, 2013. Date of publication June 5, 2013; date of current version January 16, 2014. Paper 2012-EMC-686.R1, presented at the 2012 IEEE Energy Conversion Congress and Exposition, Raleigh, NC, USA, September 15–20, and approved for publication in the IEEE TRANSACTIONS ON INDUSTRY APPLICATIONS by the Electric Machines Committee of the IEEE Industry Applications Society. This work was supported by the following research projects: 1) RITmare, Ricerca ITaliana per il mare (Italian Research for the sea) CUP: B91J11000740001 and 2) TESEO, Tecnologie ad alta Efficienza per la Sostenibilità Energetica ed ambientale On-board (High efficiency technologies for on-board energy and environmental sustainability) CUP: B61C12000850005.

The author is with the Institute of Intelligent Systems for Automation (ISSIA–CNR), 90121 Palermo, Italy (e-mail: marcello.pucci@ieee.org).

Color versions of one or more of the figures in this paper are available online at http://ieeexplore.ieee.org.

Digital Object Identifier 10.1109/TIA.2013.2266351

I. INTRODUCTION

SCIENTIFIC literature about linear induction motors (LIMs) is very large [1]–[5]. The option that LIMs offer to develop a direct linear motion without the need of any gearbox for the motion transformation (from rotating to linear) has been the key issue for their study. The counterpart of this potential advantage is the increase of complexity of the machine model, which presents the so-called end effects and border effects. These effects, which are due to asymmetries in the inductor structure with respect to the rotating machine, both in the longitudinal and transverse directions, are caused by the limited capability of the LIM drive to achieve optimal performance. It calls for proper models that can properly take into consideration these effects.

Several LIM modeling solutions have been proposed by the scientific literature. First, mathematical models of LIMs should be divided in two categories: static (valid for steady-state analysis) and dynamic. As far as static models are concerned, most of them are based on the electric circuit of the LIM, directly obtained from the rotating induction motor (RIM) counterpart, but modified so that the electrical parameters of the scheme are variable with the operating conditions. In [3, Sec. III-E], an electrical scheme of a LIM with negligible end effects is presented, where all of the electrical parameters required by the scheme are computed on the basis of the constructive elements of the LIM (pole pitch, air-gap length, thickness of the induced-part track, slot width and depth, number of turns for phases, etc.). A model of the LIM based on its electrical scheme, but properly taking into consideration the end effects, the border effect, and the induced-part skin effect (field diffusion in the secondary), has been proposed by [5]. In [5], the proposed electrical scheme is basically that of the RIM, which means that no additional passive components are present in the scheme, making this scheme suitably represent the LIM typical effects because each component of the scheme is variable with the operating condition. In fact, all of the scheme parameters are made variable with the machine speed and the supply frequency on the basis of a field analysis that can be derived with any field theory. These last two models are very accurate but present the following drawbacks: In [3], the parameters are dependent on the design data of the machine, which are hardly at the disposal of the final user (they are difficult to measure, and the companies are obviously reticent to provide this information). This kind of models can be adopted more easily by the machine designer. Reference [5] includes the end and border effects, but even in this case, the final user could not parameterize the circuit parameters with the working conditions. Reference [7] proposes an electric circuit of the LIM taking into consideration the end effects. The basic assumption of the model is definition of an end-effect factor Q, on the basis of which

some additional circuit parameters are defined, with respect to the RIM counterpart. These parameters take into consideration the global demagnetization of the machine and the additional losses in the induced-part track at increasing speed caused by the dynamic end effects. On this basis, this model also accounts for the braking force of the LIM caused by the end effects. This model presents, from the final user point of view, the advantage that the parameters of the model are those of the RIM model. Afterward, only some nonlinear functions depending on Q are to be applied to retrieve the variation laws of such parameters with the speed.

As far as dynamic models of LIMs are concerned, the main ones proposed in the literature are those in [8]–[13]. References [8] and [9] propose a dynamic model of LIM which is based on its constructional elements (pole pitch, air-gap length, thickness of the induced-part track, slot width and depth, number of turns for phases, etc.). Reference [10] focuses the application of this model in the framework of field-oriented control (FOC). The definition of this model is based on the field equations that are related to the structure of the machine and from the definition of a proper air-gap function, permitting to take into consideration both the static and dynamic end effects. It is thus particularly accurate and powerful. It is, however, hard to be adopted for control purposes from the final user since, as already stated previously, the design data of the machine are hardly at the disposal of the final user (it is difficult to measure, and the companies are obviously reticent to provide this information). It cannot be easily parameterized with a set of input–output measurements. The dynamic models in [11]–[13] are, on the contrary, space-vector-based dynamic models directly derived from [7]. All of these models do not take into consideration the static end effects, while they do consider, in different ways, the dynamic end effects.

None of these last models is, however, represented in a classic state form, which is very useful for control purposes for the definition of state estimators and observers.

This paper proposes a state space-vector model of the LIM taking into consideration the dynamic end effects. The state representation of the RIM is very well known in literature and has been properly employed for the definition of several state observers [14]–[16]. Nothing similar exists for LIMs taking into consideration the dynamic end effects.

It is directly inspired from the static model in [7], rearranged in a space-vector dynamic form. Exactly as [7], the proposed model takes into consideration the dynamic end effects, while it is not able to account for the static end effects. Same considerations can be done for the models [11]–[13], which are all derived from [7]. None of them is, however, represented in a state form.

Starting from the space-vector equivalent circuit of the LIM, the complete set of space-vector equations has been deduced. Afterward, first the so-called voltage and current flux models have been written. The definition of the flux models of the LIM, including the end effects, had already been developed by the author in [17]. In [17], however, they have been defined under the simplifying assumption that the induced-part leakage inductance was null. This assumption has been relaxed here, with a consequent more accurate definition of the flux models themselves. In [17], however, flux models had been defined for their adoption in the framework of a FOC drive with LIM, demonstrating that better dynamic performance can be achieved with the adoption a proper LIM flux model. Here, the presentation of flux models is just the starting point for the definition of a more complete state model of the LIM. This model can, in perspective, be used for control purposed for the definition of full-order Luenberger observers (LOs) or extended Kalman filters (EKFs). Some theoretical considerations about the correct field orientation conditions for LIM drives have been made by analyzing the current model in the induced-part flux reference frame. The complete expression of the net thrust generated by the LIM is presented, including the braking force term depending on the dynamic end effects. The state space-vector model has been implemented in numerical simulation and has been validated by comparing its results with both finite-element analysis (FEA) and experimental results obtained on a properly developed test set-up.

II. Space-Vector Equivalent Circuit of the LIM Including End Effects

The so-called end effects of LIMs are divided into two categories [3]: static and dynamic ones. The static end effects are caused by the fact that the inductor magnetic circuit presents an open structure. This is unavoidable because of the asymmetric positioning of the phase windings with respect to the entrance and exit of the magnetic core. As a consequence, the phase inductances are different, and the inductor currents are unbalanced, even under symmetric voltage supply. This effect can be considered negligible when the number of poles of the LIM is higher than 6 [3] and has not been taken into account in the proposed model. Some authors [18] propose to compensate the static end effects on the inductor current imbalance directly in the control action by a different choice of the $3 \rightarrow 2$ transformation matrix.

The dynamic end effects are caused by the relative motion between the short inductor and the induced-part track. This effect has been accounted for in the proposed model. In a LIM, different from a RIM, the secondary (induced part) consists of a sheet of aluminum with a back core of iron. During the motion of the inductor, a continuous variation of the aluminum sheet happens, while the inductor presents a limited length. This causes a variation of the induced currents in the sheet and corresponding magnetic flux density in the air-gap, in proximity of the entrance (front of the motion) and exit (back of the motion) of the inductor. This flux modification is different in the entrance with respect to the exit. When the moving inductor faces a new part of aluminum sheet, new induced currents are generated starting from a null value. This growth, which is quite fast because of the absence of previously induced currents, tries to oppose the inducing flux variation. The effect is a deep reduction of the resulting flux at the proximity of the entrance. At the same time, at the exit, the induced current opposes a sudden flux reduction from the inducer, creating an overall flux increase. The higher the speed of the inductor is, the higher is the end-effect phenomenon. The last one has been taken into

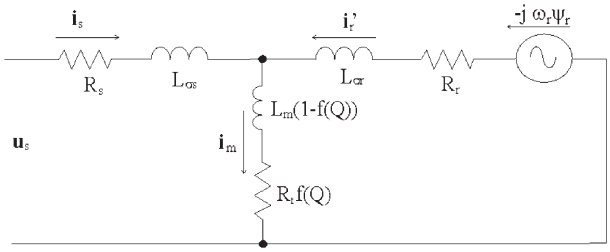

Fig. 1. Space-vector equivalent circuit of the LIM.

consideration in literature by a so-called end-effect factor Q [7], defined as

$$Q = \frac{\tau_m R_r}{(L_m + L_{\sigma r})v}. \tag{1}$$

Q is a measure of the LIM's attitude to resist the loss of output due to the end effects and is inversely proportional to the so-called goodness factor in [1] and [3]. It can be observed that, the higher the machine speed is, the higher is the air-gap thickness (higher leakage inductance), and the lower the inductor length is, the lower is factor Q. It means that the end effects increase with the machine speed and with the air-gap thickness and reduces with the inductor length.

Correspondingly, the three-phase magnetizing inductance varies with Q in the following way:

$$\hat{L}_m = L_m\ (1 - f(Q)) \tag{2}$$

with

$$f(Q) = \frac{1 - e^{-Q}}{Q} \tag{3}$$

which states that the inductance virtually reduces with the end effects accounting for an overall demagnetization of the machine.

A computation of the overall losses of the machine shows that an additional resistance appears in the transversal branch taking into consideration the eddy current joule losses. This resistance is equal to

$$\hat{R}_r = R_r f(Q). \tag{4}$$

Correspondingly, the space-vector equivalent circuit of the LIM can be deduced, as shown in Fig. 1. It could be observed that the main differences with the equivalent circuit of the RIM are in the magnetizing inductance and in the eddy current resistance, both present in the transversal branch. Fig. 2 shows the steady-state mechanical characteristic, thrust versus linear speed, under an inductor voltage of 265 V–60 Hz, of the LIM under test obtained with the classic RIM model (no end effects) and with the LIM model in Fig. 1 (with end effects). It also shows the end-effect braking force which is a quantity increasing with the LIM speed, as expected. As a result, the real characteristic of the LIM, because of the end effects, lies below the corresponding RIM and presents a no-load speed lower than the corresponding RIM. Because of the quite high value of R_r caused by the thin aluminum track, the limited value of L_m caused by the big air-gap, and the not low value of the ratio

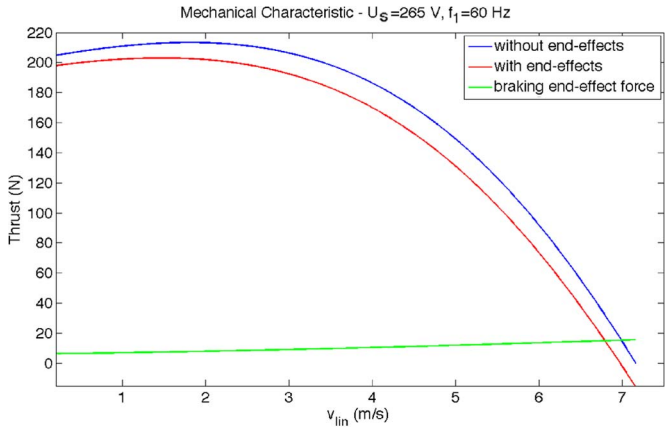

Fig. 2. Steady-state mechanical characteristic of the LIM under test.

TABLE I
PARAMETERS OF THE LIM

Rated power P_{rated} [W]	424.7
Rated voltage U_{rated} [V]	380
Rated frequency f_{rated} [Hz]	60
Pole-pairs	3
Inductor resistance R_s [Ω]	11
Inductor inductance L_s [mH]	637.6
Induced part resistance R_r [Ω]	32.57
Induced part inductance L_r [mH]	757.8
3-phase magnetizing inductance L_m [mH]	517.5
Rated thrust F_n [N]	200
Rated speed [m/s]	6.85
Mass [kg]	20

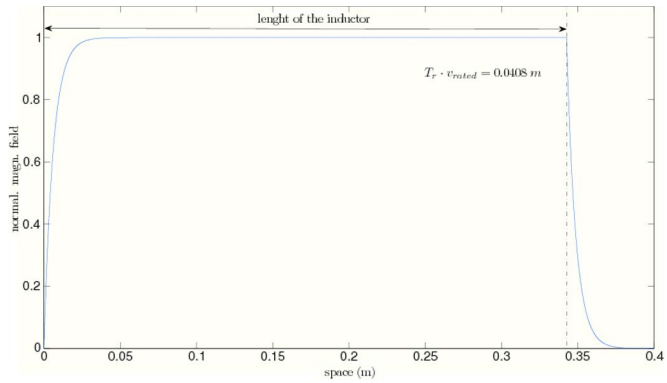

Fig. 3. Distribution of the rms value of the normalized air-gap flux density over the inductor length at rated speed.

between the inductor length and the machine rated speed, the value of Q at rated speed is not high in the machine under test, implying that the dynamic end effects are not particularly observable. This is confirmed by the distribution of the rms value of the normalized air-gap flux density over the inductor length for the LIM under test at the machine rated speed of 6.8 m/s (parameters in Table I), sketched in Fig. 3, valid under the simplifying assumptions of [7] and also valid here. It highlights that, at the machine rated speed, the demagnetizing effect of the induced-part current on the air-gap flux is already extinguished at almost one-tenth of the inductor length.

III. State Space-Vector Model of the LIM Including End Effects

Starting from the space-vector equivalent circuit in the inductor reference frame in Fig. 1, after applying the Kirchhoff law, the following set of space-vector equations of the LIM can be written, valid in the inductor reference frame:

$$\begin{cases} \mathbf{u}_s = R_s\,\mathbf{i}_s + R_r\,f(Q)\,[\mathbf{i}_s + \mathbf{i}'_r] + \frac{d\boldsymbol{\psi}_\mathbf{s}}{dt} \\ \mathbf{0} = R_r\,\mathbf{i}'_r + R_r\,f(Q)\,[\mathbf{i}_s + \mathbf{i}'_r] + \frac{d\boldsymbol{\psi}'_r}{dt} - j\omega_r\,\boldsymbol{\psi}'_r \end{cases} \quad (5a,b)$$

with

$$\begin{cases} \boldsymbol{\psi}_\mathbf{s} = [L_{\sigma s} + L_m\,(1 - f(Q))]\,\mathbf{i}_s + L_m\,(1 - f(Q))\,\mathbf{i}'_r \\ \boldsymbol{\psi}'_r = L_m\,(1 - f(Q))\,\mathbf{i}_s + [L_{\sigma r} + L_m\,(1 - f(Q))]\,\mathbf{i}'_r \end{cases} \quad (6a,b)$$

where $\mathbf{u}_s$, $\mathbf{i}_s$, $\mathbf{i}'_r$, $\boldsymbol{\psi}_\mathbf{s}$, and $\boldsymbol{\psi}'_r$ are, respectively, the inductor voltage and current, the induced-part current, and the inductor and induced-part flux linkage space vectors written in the inductor reference frame; R_s and R_r are the inductor and induced-part phase resistances; $L_{\sigma s}$ and $L_{\sigma r}$ are the inductor and induced-part leakage inductances; ω_r is the electrical rotating speed of the inductor; Q is the previously defined end-effect factor; and j is the imaginary unit. Equation (5a,b) represents, respectively, the inductor and induced-part voltage equations, while (6a,b) represents, respectively, the inductor and induced-part flux equations.

A. Voltage and Current Flux Models of the LIM

Writing (6b) as a function of $\mathbf{i}'_r$ and substituting it in (5a), the space-vector equations of the voltage model of the LIM can be deduced

$$\begin{aligned} \frac{d\boldsymbol{\psi}'_r}{dt} = {} & \frac{L_{\sigma r} + L_m\,(1 - f(Q))}{L_m\,(1 - f(Q))} \\ & \times \left\{ \mathbf{u}_\mathbf{s} - \left[R_s + R_r f(Q) - \frac{R_r f(Q) L_m\,(1 - f(Q))}{L_{\sigma r} + L_m\,(1 - f(Q))} \right] \mathbf{i}_s \right. \\ & - \hat{\sigma}\,[L_{\sigma s} + L_m\,(1 - f(Q))]\,\frac{d\,\mathbf{i}_s}{dt} \\ & \left. - \frac{R_r\,f(Q)}{L_{\sigma r} + L_m\,(1 - f(Q))}\boldsymbol{\psi}'_r \right\} \end{aligned} \quad (7)$$

where $\hat{\sigma}$ has been previously defined as

$$\hat{\sigma} = 1 - \frac{L_m^2\,(1 - f(Q))^2}{[L_{\sigma r} + L_m\,(1 - f(Q))]\,[L_{\sigma s} + L_m\,(1 - f(Q))]}.$$

$\hat{\sigma}$ is an equivalent global leakage factor taking into consideration the end effects of the LIM.

Equation (7) has been deduced under the simplifying assumption that the rate of change of the linear speed is limited, i.e., $dv/dt \cong 0$; otherwise, some additive terms depending on the linear acceleration of the motor would appear. It defines the so-called "voltage model" of the LIM, including the end effects. It should be noted that this model presents some differences with respect to the corresponding counterpart for the RIM. In particular, an additional term depending on the end-effect factor and on the induced-part flux linkage components appear. This term varies with the linear speed of the machine and is null when the linear speed of the LIM is null since the end effects are not visible in this case. Fig. 4 shows the block diagram of the voltage model of the LIM, describing (7). This flux model is an upgrade of the corresponding model in [17] since it considers the effect of the induced-part leakage inductance.

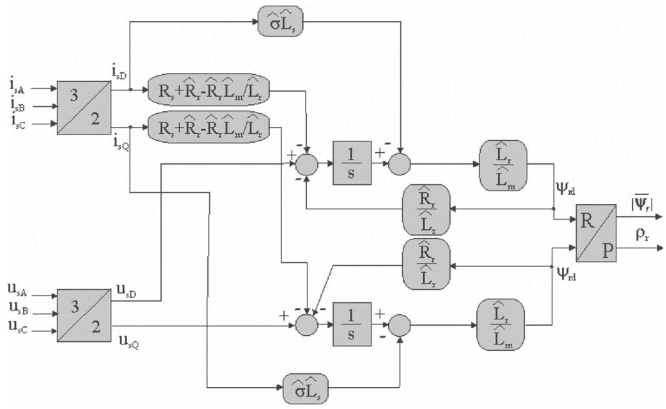

Fig. 4. Block diagram of the voltage model of the LIM.

Writing (6b) as a function of $\mathbf{i}'_r$ and substituting it in (5b), the space-vector equations of the current model can be deduced

$$\begin{aligned} \frac{d\boldsymbol{\psi}'_r}{dt} = {} & R_r \left(\frac{L_m\,(1 - f(Q))\,(1 + f(Q))}{L_{\sigma r} + L_m\,(1 - f(Q))} - f(Q) \right) \mathbf{i}_s \\ & + \left(j\frac{p\pi}{\tau_p}\,v - \frac{R_r\,(1 + f(Q))}{L_{\sigma r} + L_m\,(1 - f(Q))} \right) \boldsymbol{\psi}'_r \end{aligned} \quad (8)$$

where τ_p is the polar step of the inductor and p is the number of pole pairs. Even in this case, (8) has been deduced under the simplifying assumption that the rate of change of the linear speed is limited, i.e., $dv/dt \cong 0$. It implies that the mechanical acceleration of the LIM is not considered only in the parameter variation. It is therefore considered in the variation of the parameters with the LIM speed, while it is neglected in the effect of acceleration on the parameters. This simplifying assumption is reasonable since the mechanical time constant is much bigger than the electric one. This is particularly true for LIMs where the inductance terms are all very small because of the big air-gap and the resistances are big, particularly those of the induced-part track (limited thickness of the aluminum track). The term $(p\pi/\tau_p)v = \omega_r$ represents the equivalent rotational speed of the induced part in electrical angles. Equation (8) represents the so-called "current model" of the LIM, including the end effects. On this basis, an equivalent induced-part time constant of the machine taking into consideration the end effects, depending on the linear machine speed itself, can be defined as

$$\hat{T}_r = \frac{L_{\sigma r} + L_m\,(1 - f(Q))}{R_r\,(1 + f(Q))}. \quad (9)$$

If, for the sake of simplicity, the following modified electrical parameters of the LIM (variable with the machine speed) are

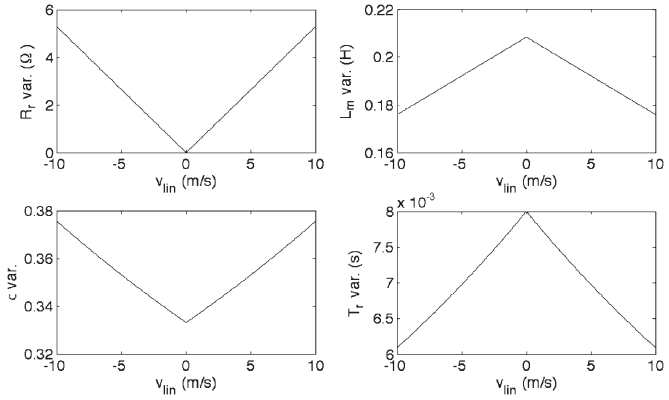

Fig. 5. Modified electrical parameters versus linear speed.

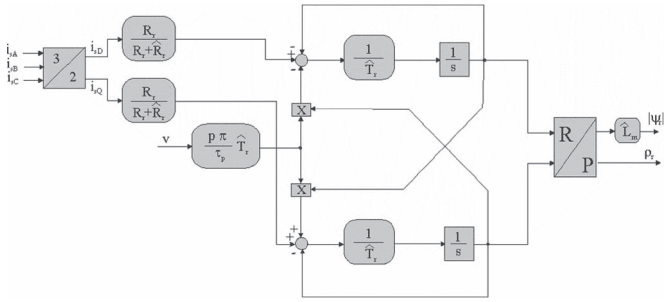

Fig. 6. Block diagram of the current model of the LIM in the inductor reference frame.

defined:

$$\hat{L}_s = L_{\sigma s} + L_m\ (1 - f(Q)) \quad \hat{L}_r = L_{\sigma r} + L_m\ (1 - f(Q))$$

then (7) and (8) can be rewritten in a more compact form. These parameters have also a clear physical meaning.

As far as the LIM under test is concerned (parameters in Table I), Fig. 5 shows the variations with the linear speed v of the parameters $\hat{R}_r$, $\hat{L}_m$, $\hat{\sigma}$, and $\hat{T}_r$. It could be noted that, in accordance with the definition of Q, the higher the machine speed is, the higher are the values of $\hat{R}_r$ and $\hat{\sigma}$ and the lower are the values of $\hat{L}_m$ and $\hat{T}_r$. It should be further noted that, in the machine under test, the variation of the parameters with the LIM speed is limited, according to the limited presence of the dynamic end effects in the machine under test (see Fig. 3). More significant variations of these parameters are to be expected in machines with more present end effects.

Fig. 6 shows the block diagram of the current model of the LIM in the inductor reference frame, describing (8) under further simplification

$$\frac{\hat{R}_r \hat{T}_r}{\hat{L}_m} \cong \frac{\hat{R}_r}{R_r + \hat{R}_r} = \frac{f(Q)}{1 + f(Q)} \tag{10}$$

deriving from the assumption that the induced-part leakage inductance is negligible: $L_{\sigma r} \cong 0$. Without this last simplification, the corresponding block diagram would become much more complicated. Even in this case, the dependence on the machine speed is visible in all of the parameters with the $\hat{}$.

If (8) is transformed from the inductor to the induced-part flux linkage reference frame by the vector rotation $\boldsymbol{\psi}_r^{\psi_r} = \boldsymbol{\psi}_r' e^{-j\rho_r}$, where ρ_r is the induced-part flux angle, the following space-vector equation can be deduced:

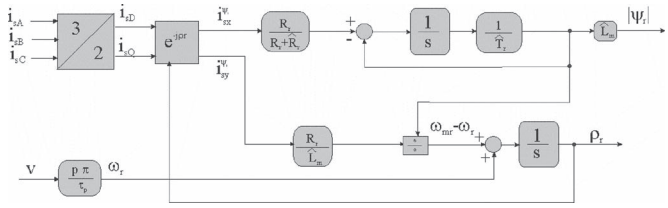

Fig. 7. Block diagram of the current model of the LIM in the induced-part flux reference frame.

$$\frac{d\,\boldsymbol{\psi}_r^{\boldsymbol{\psi}_r}}{dt} + \frac{1}{\hat{T}_r}\,\boldsymbol{\psi}_{\mathbf{r}}^{\boldsymbol{\psi}_{\mathbf{r}}} = \left(\frac{\hat{L}_m}{\hat{T}_r} - \hat{R}_r\right)\mathbf{i}_s^{\boldsymbol{\psi}_{\mathbf{r}}} - j\left(\omega_{mr} - \frac{p\pi}{\tau_p}\,v\right)\boldsymbol{\psi}_{\mathbf{r}}^{\boldsymbol{\psi}_{\mathbf{r}}} \tag{11}$$

where the term ψ_{r} in apex means that the variable is expressed in the induced-part reference frame and ω_{mr} is the induced-part flux vector rotational speed. If (11) is decomposed in its real and imaginary parts, under the same assumption $\hat{R}_r\hat{T}_r/\hat{L}_m \cong \hat{R}_r/(R_r + \hat{R}_r) = f(Q)/(1 + f(Q))$, the two following scalar equations could be obtained:

$$\begin{cases} \frac{\hat{T}_r}{\hat{L}_m}\frac{d|\boldsymbol{\psi}_{\mathbf{r}}|}{dt} + \frac{1}{\hat{L}_m}|\boldsymbol{\psi}_{\mathbf{r}}| = \frac{R_r}{R_r + \hat{R}_r}\, i_{sx}^{\boldsymbol{\psi}_{\mathbf{r}}} \\ \omega_{mr} = \frac{p\pi}{\tau_p}v + \frac{R_r i_{sy}^{\boldsymbol{\psi}_{\mathbf{r}}}}{|\boldsymbol{\psi}_{\mathbf{r}}|}. \end{cases} \tag{12 a, b}$$

Equation (12) defines the "current model" in the induced-part flux linkage reference frame. In particular, (12a) confirms that the induced-part flux amplitude depends only on the direct component of the inductor current and its dynamics depends on the previously defined equivalent induced-part time constant $\hat{T}_r$, which is a varying quantity with the linear speed. Equation (12b) confirms that the slip speed, from which the steady-state value of thrust directly depends, has a direct proportionality with the quadrature component of the inductor current. Equation (12) basically defines the correct conditions of field orientation for a LIM. Fig. 7 shows the block diagram of the "current model" of the LIM in the induced-part flux reference frame, describing (12).

Some important consideration should be made about the field orientation conditions in LIMs and RIMs. From (12), it is possible to deduce the ratios between the induced-part flux amplitudes and the slip speeds, computed, respectively, with the aforementioned model (called LIM) and with the classic model for the rotating machine (called RIM)

$$\begin{cases} \frac{|\boldsymbol{\psi}_{\mathbf{r}}|_{\mathrm{LIM}}}{|\boldsymbol{\psi}_{\mathbf{r}}|_{\mathrm{RIM}}} = \frac{1-f(Q)}{1+f(Q)} \\ \frac{\omega_{sl\ \mathrm{LIM}}}{\omega_{sl\ \mathrm{RIM}}} = \frac{1+f(Q)}{1-f(Q)}. \end{cases} \tag{13}$$

Fig. 8 shows, for the machine under test, the plots drawing (13). It can be observed that not considering the end effects in the estimation of the flux implies that, at the machine rated speed, an overestimation of the flux amplitude of almost 20% and an underestimation of the slip speed of about 20% as well are to be expected. This percentage is quite high even with a LIM where the dynamic end effects are poorly visible. It implies that even limited end effects influence significantly the field orientation capability of the LIM drive.

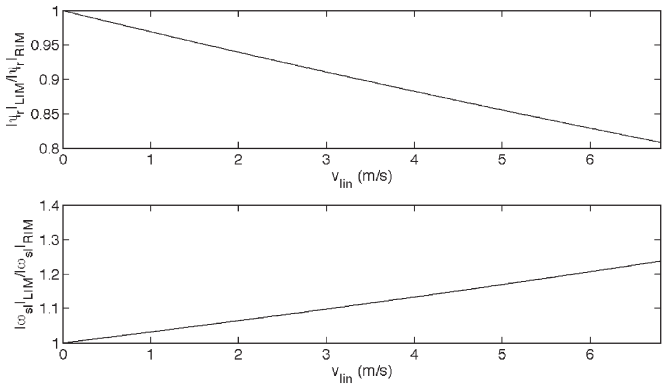

Fig. 8. $|\boldsymbol{\psi}_\mathbf{r}|_{\mathrm{LIM}}/|\boldsymbol{\psi}_\mathbf{r}|_{\mathrm{RIM}}$ and $\omega_{sl\ \mathrm{LIM}}/\omega_{sl\ \mathrm{RIM}}$ versus speed.

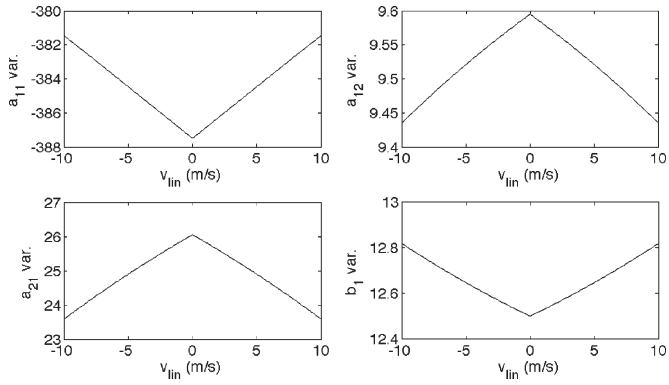

Fig. 9. State model parameters versus linear speed.

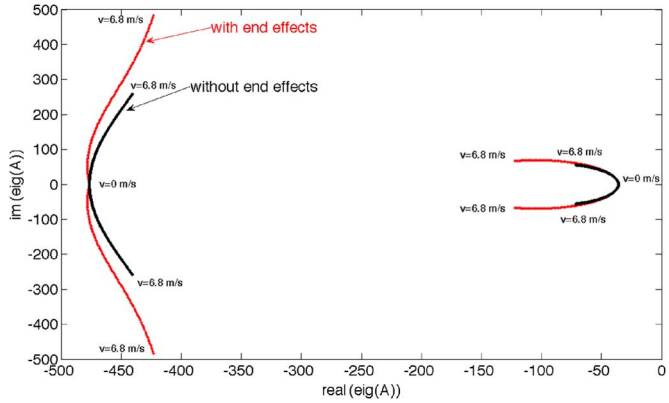

Fig. 10. Poles of the LIM with and without considering the end effects.

B. State-Space Space-Vector Model of the LIM

To deduce the state representation of the space-vector model of the LIM taking into consideration the end effects, the first space-vector equation to be considered is the voltage model represented in (7), which must be rewritten as a function of $d\,\mathbf{i}_s/dt$, after substituting the expression of $d\,\boldsymbol{\psi}'_\mathbf{r}/dt$ taken from the current model of (8). The second space-vector equation is given directly by the current model, represented in (8). As a result, the following set of two space-vector equations can be obtained:

$$\frac{d\,\mathbf{i}_s}{dt} = \frac{1}{\hat{\sigma}\hat{L}_s}\left\{\mathbf{u}_s - \left[R_s + \hat{R}_r\left(1-\frac{\hat{L}_m}{\hat{L}_r}\right) + \frac{\hat{L}_m}{\hat{L}_r}\left(\frac{\hat{L}_m}{\hat{T}_r} - \hat{R}_r\right)\right]\mathbf{i}_s - \frac{\hat{L}_m}{\hat{L}_r}\left[j\frac{p\pi}{\tau_p}\,v - \frac{1}{\hat{T}_r} - \frac{\hat{R}_r}{\hat{L}_m}\right]\boldsymbol{\psi}'_\mathbf{r}\right\} \tag{14}$$

$$\frac{d\boldsymbol{\psi}'_\mathbf{r}}{dt} = \left[\frac{\hat{L}_m}{\hat{T}_r} - \hat{R}_r\right]\mathbf{i}_s + \left[j\frac{p\pi}{\tau_p}\,v - \frac{1}{\hat{T}_r}\right]\boldsymbol{\psi}'_\mathbf{r}. \tag{15}$$

The final full-state space-vector set of equations, written in matrix form where all of the space vectors become two-element vectors composed by the corresponding direct and quadrature components, is therefore

$$\frac{d}{dt}\begin{bmatrix}\mathbf{i_s}\\ \boldsymbol{\psi}'_\mathbf{r}\end{bmatrix} = \begin{bmatrix}\mathbf{A_{11}} & \mathbf{A_{12}}\\ \mathbf{A_{21}} & \mathbf{A_{22}}\end{bmatrix}\begin{bmatrix}\mathbf{i_s}\\ \boldsymbol{\psi}'_\mathbf{r}\end{bmatrix} + \begin{bmatrix}\mathbf{B_1}\\ \mathbf{0}\end{bmatrix}\mathbf{u_s} = \mathbf{A}\mathbf{x} + \mathbf{B}\mathbf{u_s} \tag{16a}$$

$$\mathbf{i_s} = \mathbf{C}\mathbf{x} \tag{16b}$$

where $\mathbf{C} = [\mathbf{I} \quad \mathbf{0}]$, $\mathbf{I} = \begin{bmatrix}1 & 0\\ 0 & 1\end{bmatrix}$, $\mathbf{J} = \begin{bmatrix}0 & -1\\ 1 & 0\end{bmatrix}$, and

$$\mathbf{A}_{11} = a_{11}\mathbf{I} = -\frac{1}{\hat{\sigma}\hat{L}_s}\left[R_s + \hat{R}_r\left(1-\frac{\hat{L}_m}{\hat{L}_r}\right) + \frac{\hat{L}_m}{\hat{L}_r}\left(\frac{\hat{L}_m}{\hat{T}_r} - \hat{R}_r\right)\right]\mathbf{I} \tag{17a}$$

$$\mathbf{A}_{12} = a_{12}\left[\left(\frac{1}{\hat{T}_r} + \frac{\hat{R}_r}{\hat{L}_m}\right)\mathbf{I} - \frac{p\pi}{\tau_p}\,v\,\mathbf{J}\right] = \frac{\hat{L}_m}{\hat{\sigma}\hat{L}_s\hat{L}_r}\left[\left(\frac{1}{\hat{T}_r} + \frac{\hat{R}_r}{\hat{L}_m}\right)\mathbf{I} - \frac{p\pi}{\tau_p}\,v\,\mathbf{J}\right] \tag{17b}$$

$$\mathbf{A}_{21} = a_{21}\mathbf{I} = \left(\frac{\hat{L}_m}{\hat{T}_r} - \hat{R}_r\right)\mathbf{I} \tag{17c}$$

$$\mathbf{A}_{22} = a_{22}\left[\frac{1}{\hat{T}_r}\mathbf{I} - \frac{p\pi}{\tau_p}\,v\,\mathbf{J}\right] = -1\left[\frac{1}{\hat{T}_r}\mathbf{I} - \frac{p\pi}{\tau_p}\,v\,\mathbf{J}\right] \tag{17d}$$

$$\mathbf{B}_1 = b_1\mathbf{I} = \frac{1}{\hat{\sigma}\hat{L}_s}\mathbf{I}. \tag{17e}$$

The coefficients of the state representation depend, in this case, on the linear speed of the LIM. As far as the LIM under test is concerned (parameters in Table I), Fig. 9 shows the variations with the linear speed v of the parameters of the state representation. Coherently with what stated previously, these parameters do not vary a lot with the machine speed due to the limited presence of the end effects in the machine under test.

It can finally be observed that, if the end effects were not considered $(Q = 0)$, the coefficients of the LIM state space-vector equation would coincide with those of the classic RIM [14], [15]. Fig. 10 shows the locus described on the complex plane by the poles of the LIM under test, corresponding to the eigenvalues of the matrix $\mathbf{A}$, for different values of the linear speed (drawn for v ranging from -6.8 to 6.8 m/s). This graph has been plotted twice, respectively, without considering the LIM dynamic end effects (state parameters constant), as well as considering them (state parameters variable).

Some interesting considerations about the dynamics of the LIM could be done by observing the locus of its poles; these considerations can be extended to similar cases. First, the poles related to the induced-part flux are positioned more on the left than those related to the inductor current. It means that the

dynamics of the induced-part flux is faster than that of the inductor current. This is the dual situation with respect to the typical RIM dynamics and is due to the very low induced-part time constant of the LIM.

Moreover, the presence of the end effects causes an increase of the amplitude of the poles for a given speed, particularly for the poles related to the inductor current (right branch of the locus), corresponding to a fastening of the related dynamics caused by the reduction of the transient time constant. At the same time, a reduction of the damping factor occurs, particularly for the poles related to the induced-part flux linkage (left branch of the locus). These effects can be even more significant in LIMs with more pronounced end effects.

C. Mechanical Equation

The mechanical equation of the motion of a LIM is

$$F = F_L + F_r + M\frac{dv}{dt} \tag{18}$$

where F is the net thrust produced by the LIM; F_r is the friction force, frequently varying with the speed v by a nonlinear low value; F_L is the load force; and M is the overall mass of the system (motor plus payload). Different from the RIM, in the LIM case, the net force is the algebraic sum of the electromagnetic force F_e (analogous to the torque expression of the RIM) and the braking force due to the end effects F_{eb}.

The well-known expression of the LIM thrust is the following:

$$F_e = \frac{3}{2}\frac{\pi}{\tau_p}\frac{\hat{L}_m}{\hat{L}_r}\left|\boldsymbol{\psi}'_r\right| \mathbf{i}_{sy} \tag{19}$$

where the inductance terms are with the $\hat{}$ symbol, which means that they are quantities depending on the machine speed v.

The expression of the braking force caused by the dynamic end effects of the LIM can be found starting from the active power dissipated as Joule effect on the additional resistance $\hat{R}_r = R_r f(Q)$ in the transversal branch of the equivalent circuit of the LIM (Fig. 1). This power can be written as

$$P_{eb} = \frac{3}{2}R_r\, f(Q)\, \Re e\left(\mathbf{i}_m \mathbf{i}^*_m\right) \tag{20}$$

where $\mathbf{i}_\mathrm{m}$ is the magnetizing current space vector and * indicates the complex conjugate operator. If the inductor and induced-part flux equations are exploited, the magnetizing space vector can be rewritten as a function of the inductor current and the induced-part flux linkage

$$\mathbf{i}_m = \frac{1}{\hat{L}_r}\boldsymbol{\psi}'_r + \left(1 - \frac{\hat{L}_m}{\hat{L}_r}\right)\mathbf{i}_s. \tag{21}$$

After substituting (21) in (20), the expression of the active power dissipated because of the end effect can be found as

$$P_{eb} = \frac{3}{2}R_r\, f(Q)\left[\frac{\left|\boldsymbol{\psi}'_r\right|^2}{\hat{L}_r^2} + \left(1 - \frac{\hat{L}_m}{\hat{L}_r}\right)^2 |\mathbf{i}_s|^2 + \frac{1}{\hat{L}_r}\left(1 - \frac{\hat{L}_m}{\hat{L}_r}\right)\boldsymbol{\psi}'_r \circ \mathbf{i}_s\right]. \tag{22}$$

Correspondingly, the braking force due to the end effects can be found as

$$F_{eb} = \frac{P_{eb}}{v} = \frac{3}{2}\frac{L_r\left(1 - e^{-Q}\right)}{p\,\tau_p} \times \left[\frac{\left|\boldsymbol{\psi}'_r\right|^2}{\hat{L}_r^2} + \left(1 - \frac{\hat{L}_m}{\hat{L}_r}\right)^2 |\mathbf{i}_s|^2 + \frac{1}{\hat{L}_r}\left(1 - \frac{\hat{L}_m}{\hat{L}_r}\right)\boldsymbol{\psi}'_r \circ \mathbf{i}_s\right]. \tag{23}$$

Equation (23) depends on the machine speed, changing its sign with it and being always subtractive with respect to the propulsion force. Moreover, at zero speed, this force is nonnull and is proportional to the square of the induced-part flux amplitude as well as to the inner (dot) product between the induced-part flux and inductor current.

IV. Comparison With Other Dynamic Models in Literature

Some considerations should be made about the advantages and disadvantages of the proposed space-vector state model with respect to other dynamic models of LIMs present in the scientific literature. As far as the advantages are concerned, the following points should be highlighted.

1) It is simple and not cumbersome from the computational point of view. In this sense, it is much lighter than other space-vector models taking into consideration the end effects as [8]–[10], which are based on the definition of a set of space harmonics of the magnetomotive force (MMF) obtained by a proper representation of the air-gap function.
2) It offers a state formulation, which makes it naturally adoptable for control purposes, e.g., to develop reduced-order observers, LOs, and EKFs. In this sense, it is much more exploitable than [8]–[10], which present a completely different approach, and even of [11]–[13], which, starting from the same equivalent circuit, do not process the equation toward a state formulation.
3) It is the natural extension of the corresponding space-vector state model of the RIM to the LIM case taking into consideration the end effects, and does not present a completely different formulation. Its reliability is thus more easily evaluable.
4) It is based, as the classic model of the RIM, only on electric quantities (resistance and inductance terms), which are measurable quantities by classic tests. As a consequence, it does not require any knowledge of constructive elements of machines (number of slots, number of coils for slot, thickness of the induced-part track, air-gap length, etc.); these are design data which companies hardly provide to the user and which cannot easily be measured by input–output tests. This is, on the contrary, the case of the model in [8]–[10]. From this point of view, the approach is the same as that in [11]–[13].

The main drawback of the proposed model is that it is not able to account for the static end effects, while it takes

into consideration the dynamic end effects by the definition of factor Q. This factor is defined on the basis of the spatial representation, on the longitudinal direction of the LIM, of the rms value of the inductor MMF profile caused by the sudden growth of new currents in the induced-part track. In this regard, it permits to account the overall demagnetization of the machine caused by the end effects at increasing speeds. This effect, being computed over the entire length of the machine where all the phase windings lie, must thus be symmetrically spread on the three phases. As a result, it does not represent the static end effects since it does offer any representation of the space harmonics of the MMF due to the varying air-gap in proximity to the ending parts of the inductor. Neither in [12], the static end effects are accounted for, where the same sets of initial flux linkage space-vector equations of LIM as here are written [12, eqs. (11)–(14)], describing the same magnetic symmetry among the phases. Since the $R_r\ f(Q)$ resistance term (see Fig. 1) is neglected in the model in [12], the braking force of the LIM is not accounted for, different from here.

An attempt to include the static end effects in the dynamic end-effect definition has been made by [11] and [13]. They both start from the steady-state equivalent circuit of the LIM developed by [7] but arbitrarily decide to apply the variable inductance $L_m\ (1 - f(Q))$ responsible of the reduction of the magnetizing inductance only on the direct axis, leaving the quadrature axis free from this effect. On this basis, [11] and [13] derive a set of electromagnetic equations of the machine which are different on the direct and quadrature axes, including the braking force due to the end effect. This choice is, in the author's opinion, quite arguable. As a matter of fact, the variable inductance $L_m\ (1 - f(Q))$ accounts for the overall machine demagnetization and is computed on the basis of the rms distribution of the MMF over the entire length of the machine where all the phase windings lie. It implies that this inductance term must be symmetrically spread over the three phases, as confirmed by [12]. Moreover, on the basis of the assumptions in [7], the $L_m\ (1 - f(Q))$ term must be interested by the entire magnetizing current, both the direct and quadrature axes, and not only by one of its components as in [11] and [13].

The static and dynamic end effects are, on the contrary, fully and properly described by the model in [8]–[10], where the static end effects are automatically taken into account by the air-gap function definition, accounting for the presence of different space harmonics of the MMF on the three phases.

V. Test Set-Up

A test set-up has been suitably built to validate the state space-vector dynamic model taking into consideration the LIM end effects. The machine under test is a LIM model Baldor LMAC1607C23D99, whose rated data and electrical parameters are shown in Table I. The LIM has been equipped with a linear encoder Numerik Jena LIA series. The LIM presents an induced-part track with a length of 1.6 m.

The employed test set-up consists of the following:

1) a three-phase LIM with parameters shown in Table I;

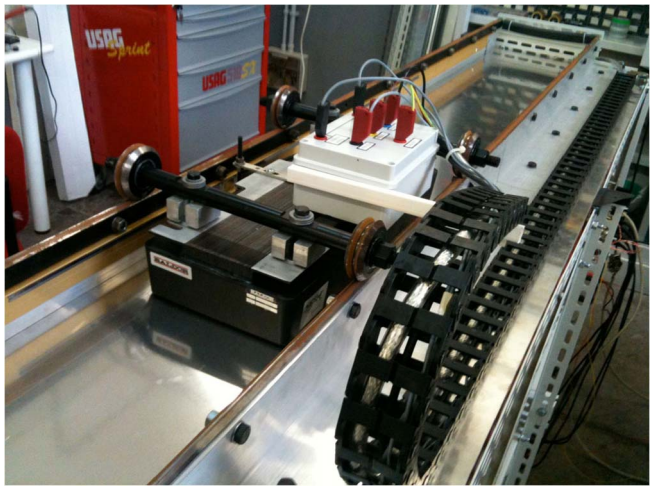

Fig. 11. Photograph of the experimental test set-up.

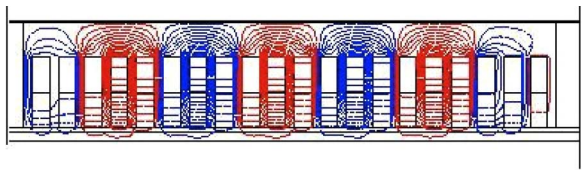

Fig. 12. Flux density contour lines at steady state.

2) a frequency converter which consists of a three-phase diode rectifier and a 7.5-kVA three-phase voltage source inverter (VSI);
3) a dSPACE card (DS1103) with a PowerPC 604e at 400 MHz and a floating-point DSP TMS320F240.

Fig. 11 shows a photograph of the test set-up.

VI. FEA Validation of the Model

The proposed state space-vector model of the LIM taking into consideration the end effects has been validated by comparing the results obtained with its numerical simulation with the FEA results. To highlight the improvements achievable with the LIM model taking into consideration the end effect, results have been further compared with those obtained with the classic space-vector model not considering the end effects (hereafter called RIM model for the sake of simplicity). The parameters of the LIM adopted for the numerical simulation are those in Table I. The proposed state space-vector model has been implemented in MATLAB–Simulink environment. The LIM under tests has been modeled by the FEA software FLUX-2D from CEDRAT. Currently, only a 2-D transient analysis has been performed. It should be noted that, for such tests, the machine mass has been reduced to one-third of that of the real machine; it has been made because there is a limitation in the maximum possible length of the induced-part tack which can be simulated with the FLUX-2D software. With the real mass of the LIM, it could not get the steady-state speed at its rated frequency. This reduction of the simulated mass obviously does not modify the goodness of the validation.

A step speed reference of 6.8 m/s (rated speed) has been provided to the machine, corresponding to an inductor supply voltage of 265 V, 60 Hz at no load. Fig. 12 shows the flux

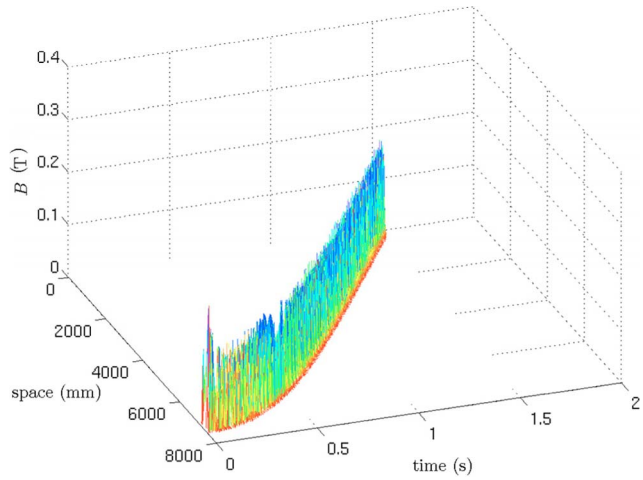

Fig. 13. Flux density versus time and distance.

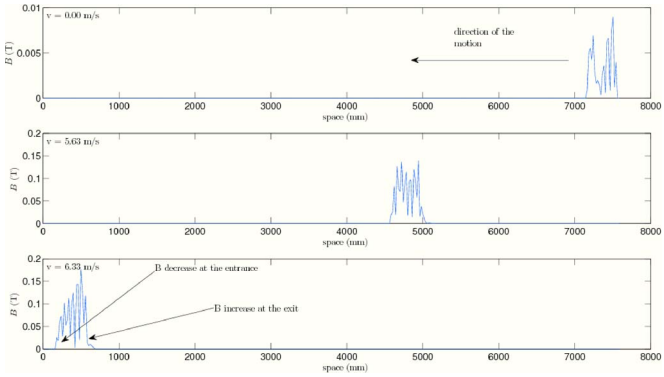

Fig. 14. Flux density distribution versus distance.

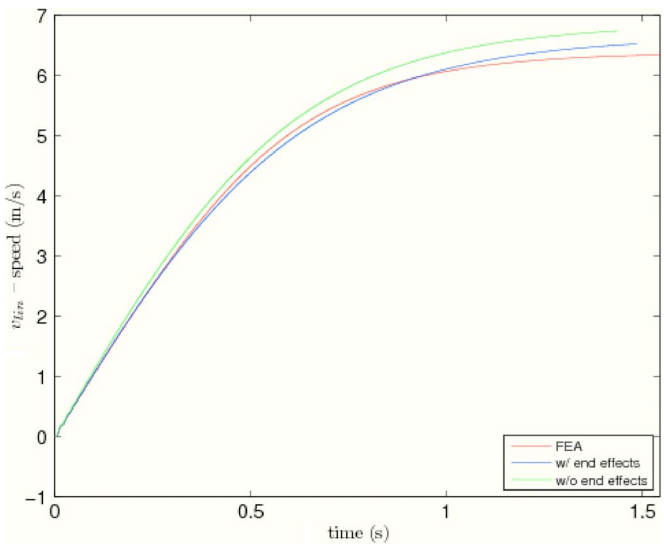

Fig. 15. Linear speed for a speed step of 6.8 m/s.

density lines obtained at the steady-state speed of 6.8 m/s. Fig. 13 shows the 3-D surface describing the flux density versus the distance of the inductor and the time (FEA). Fig. 14 shows three flux density plots, obtained, respectively, at low, medium, and high speed (FEA); these represent basically three slices of the surface in Fig. 14. From Fig. 14, the field reduction at the entrance of the motion and its increase at the exit of the motion are clearly visible. These effects increase with the speed, as

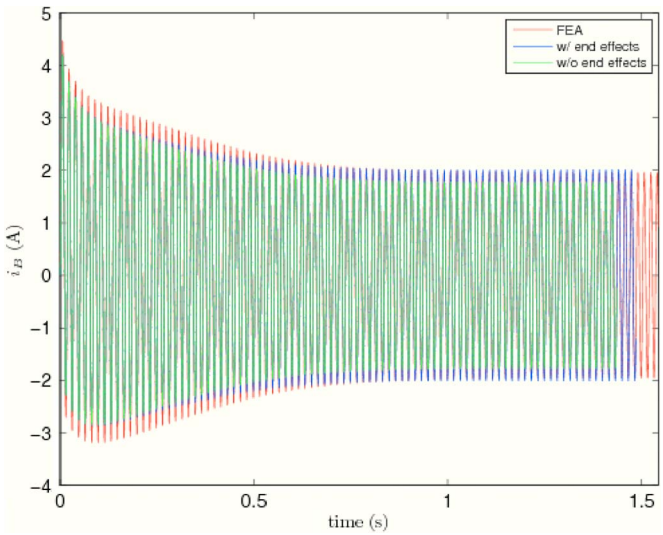

Fig. 16. Inductor phase currents for the speed step of 6.8 m/s.

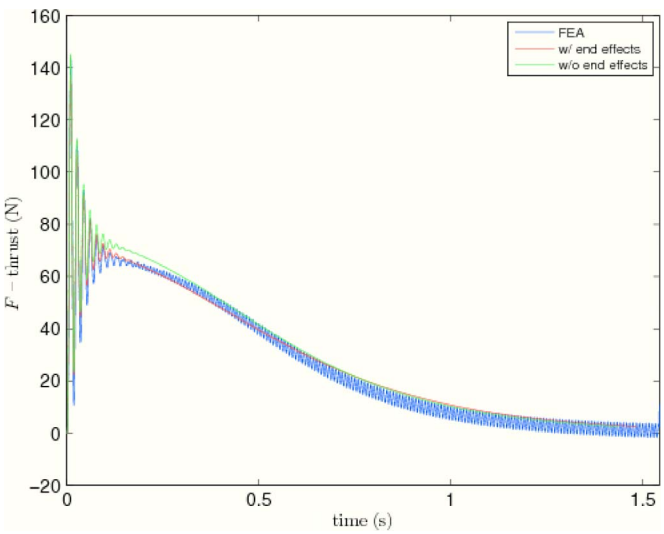

Fig. 17. Thrust for the speed step of 6.8 m/s.

a result of the presence of the end effects. Figs. 15–17 show, respectively, the LIM linear speed, the inductor phase current, and the net electromagnetic force, obtained with the FEA, with the proposed state space-vector model including the end effects and with the classic model not considering the end effects. In this regard, some considerations should be made. As far as the speed curve is concerned, it can be noted that the proposed model better matches the FEA than the classic model during the whole transient; in particular, the steady-state value of the speed obtained with the proposed model is much closer to the FEA than the classic RIM model. This is due to the fact that the proposed model takes implicitly into consideration the steady-state slip speed caused by the braking force due to the end effects. This is not the case of the classic RIM model. As far as the inductor phase current is concerned, it can be observed that the steady-state value of the current obtained with the proposed model is perfectly superimposed to the FEA, different from the classic RIM model. This is due to the fact that the proposed model takes into consideration the overall demagnetization of the machine at high speed due to the end

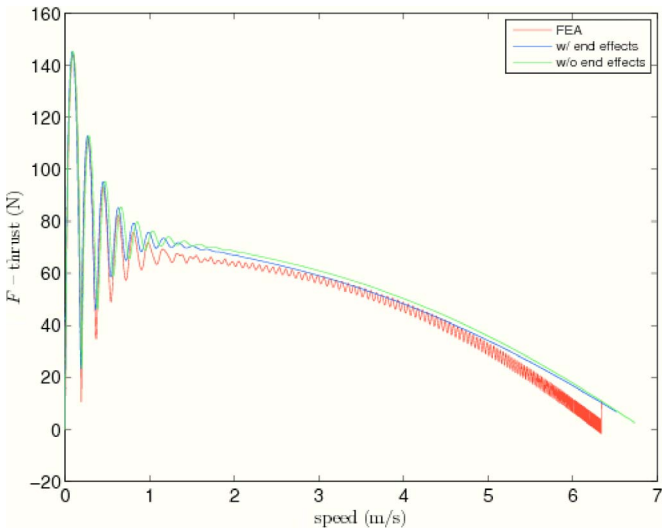

Fig. 18. Mechanical dynamic characteristic for the speed step of 6.8 m/s.

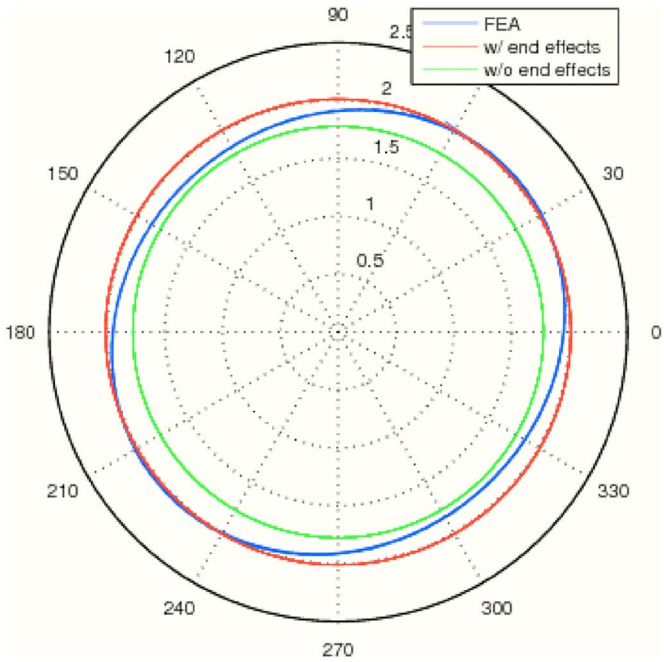

Fig. 19. Inductor current space-vector steady-state locus.

effects (reduction of the $\hat{L}_m$ term with the speed). The thrust curve shows that the net thrust estimated by the proposed model perfectly matches with the FEA, even during the initial fast transient. The classic RIM model presents a bias in the force estimation during the transient. This is due to the fact that the proposed model takes into consideration the braking force due to the end effect. This is not the case of the classic RIM model. Fig. 18 shows the dynamic mechanical characteristic of the LIM, net force versus machine speed. Even in this case, the results obtained with the proposed model better matches the FEA ones, particularly in the high-speed region, where the classic model not considering the end effects overcomes the FEA and the proposed model final point in terms of steady-state final speed. Finally, Fig. 19 shows the steady-state inductor current locus at the speed of 6.8 m/s. It can be observed that the locus obtained by FEA presents a classic asymmetry (it

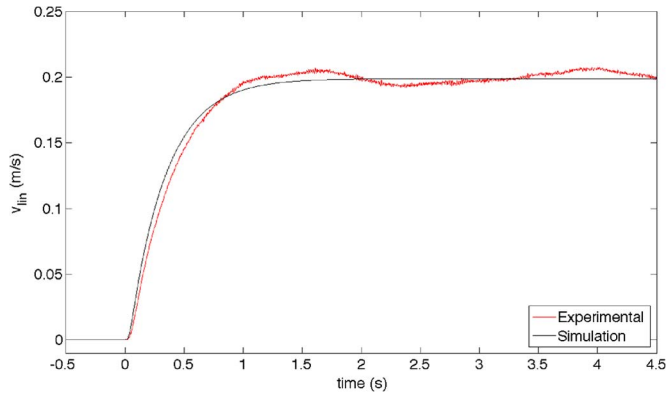

Fig. 20. Linear speed for the speed step of 0.6 m/s.

becomes an ellipse instead of a circle as in the RIM case) due to the static end effects. However neither the proposed model nor the classic RIM model is able to reproduce the static end effects, as expected. As a result, both loci present a circular shape. The inductor current locus obtained with the proposed model, however, perfectly matches the FEA one in some parts, moving away from it in others. On the contrary, the locus obtained with the classic RIM model does not match the FEA one.

It should be finally noted that, even if the differences between the proposed model and the classic RIM model are not always very big, they are observable and significant on the inductor current and the machine speed waveforms. As already stated, the LIM under tests presents limited end effect (Q not very high). More significant differences between the proposed model and that of the RIM are to be expected with machines with higher values of Q (lower values of the goodness factor) present, better justifying the end effects to be accounted in the model.

VII. Experimental Validation of the Model

The proposed state space-vector model of the LIM taking into consideration the end effects has been also experimentally validated, adopting the test set-up described in Section V. Even in this case, the parameters of the LIM adopted for the numerical simulation are those in Table I. The LIM, both in the numerical simulation and in the experiment, has been supplied with an open-loop voltage/frequency scalar-controlled VSI, driven by a space-vector pulsewidth modulation technique ($f_{\mathrm{PWM}} = 5$ kHz). Three step speed references of 0.6, 0.9, and 1.8 m/s (not higher because of the limited length of the induced-part track) have been provided to the LIM. It should be considered that the motor is intrinsically loaded with the friction force caused by its weight insisting on the guide (Fig. 3).

This has been considered in the numerical model with a load force linearly varying with the LIM speed. Figs. 20 and 21 show the simulated and experimental linear speeds obtained during the 0.6- and 0.9-m/s step test, respectively. It can be observed that the final steady-state value of the speed is about 0.2 m/s, with a corresponding slip value of about 66.7% (47.7%). The simulated speed properly tracks the experimental measurement during both transient and steady state. Figs. 22 and 23 show the corresponding waveforms of the inductor phase currents,

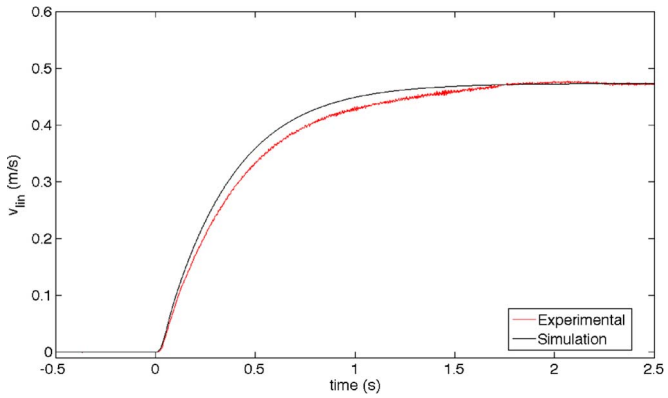

Fig. 21. Linear speed for the speed step of 0.9 m/s.

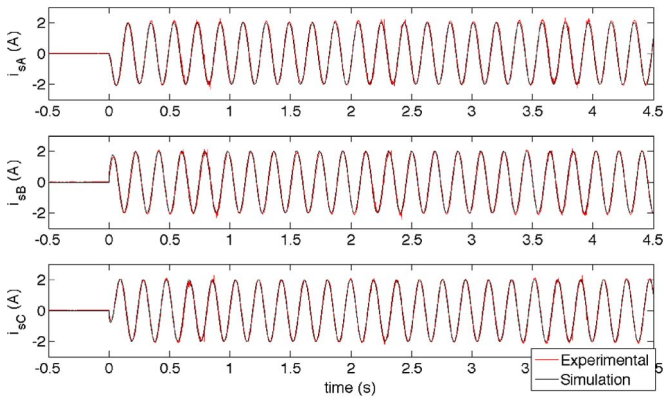

Fig. 22. Inductor phase currents for the speed step of 0.6 m/s.

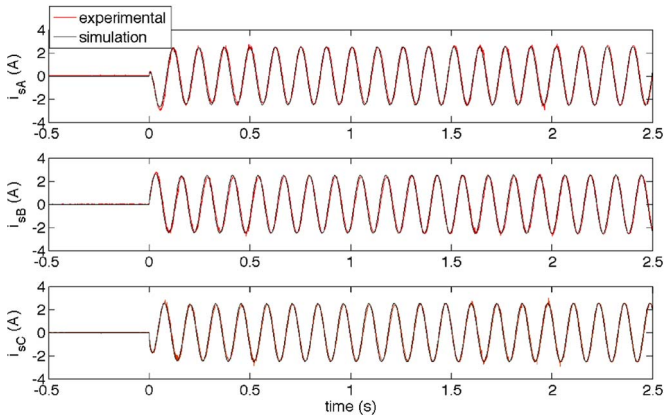

Fig. 23. Inductor phase currents for the speed step of 0.9 m/s.

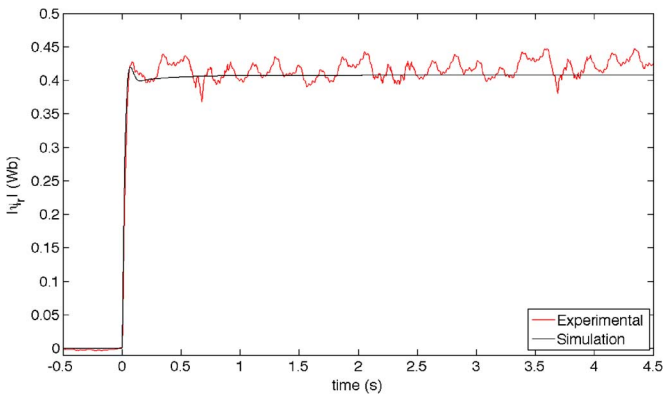

Fig. 24. Induced-part flux linkage for the speed step of 0.6 m/s.

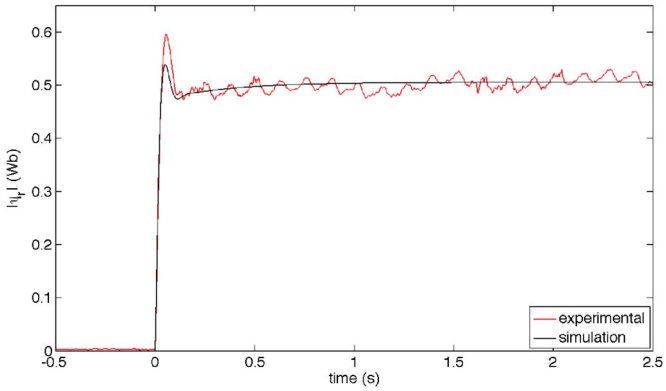

Fig. 25. Induced-part flux linkage for the speed step of 0.9 m/s.

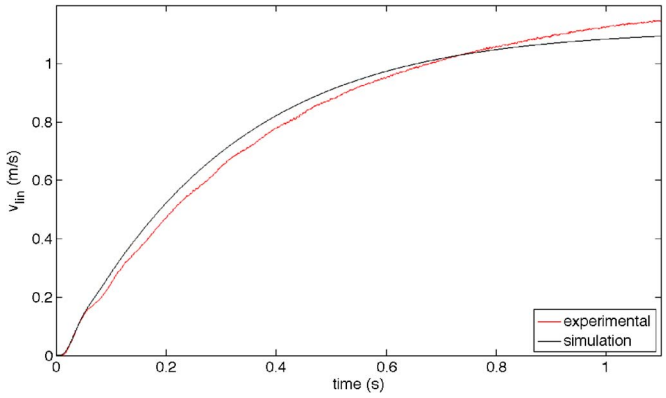

Fig. 26. Linear speed for the speed step of 1.8 m/s.

respectively, for the simulated and experimental ones. Even in this case, it could be noted how the simulated waveforms properly track the experimental ones during both transient and steady state. Figs. 24 and 25 show the amplitudes of the induced-part flux linkages, respectively, in the numerical simulation and in the experiment. Even in this case, there is a good agreement between the simulated results.

Finally, Figs. 26–28 show the same waveforms obtained under the 1.8-m/s step test. Even in this case, a good agreement between the simulated and experimental results can be observed. Fig. 29 shows, under these working conditions, the electromagnetic thrust and the load force. The load force increases with the LIM speed, as expected, matching the electromagnetic thrust at steady-state speed, where a slip equal to 38.8% occurs. Fig. 30 shows the modified electrical parameters of the LIM, as defined in Section III. As expected, $\hat{R}_r$ increases with the LIM speed, $\hat{L}_m$ reduces with it, $\hat{\sigma}$ increases with it, and finally, $\hat{T}_r$ reduces with it. Finally, Fig. 31 shows the time variation of the state space-vector model parameters with the LIM speed. It can be noted that a_{11} and b_1 increase with the speed, while a_{12} and a_{21} reduce with it. As recalled previously, the state space-vector model parameters present, in this particular case, slight variations with the machine speed because of the limited value of the dynamic end effects.

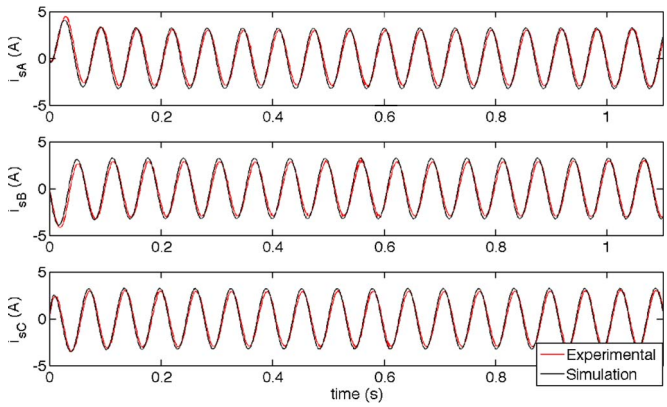

Fig. 27. Inductor phase currents for the speed step of 1.8 m/s.

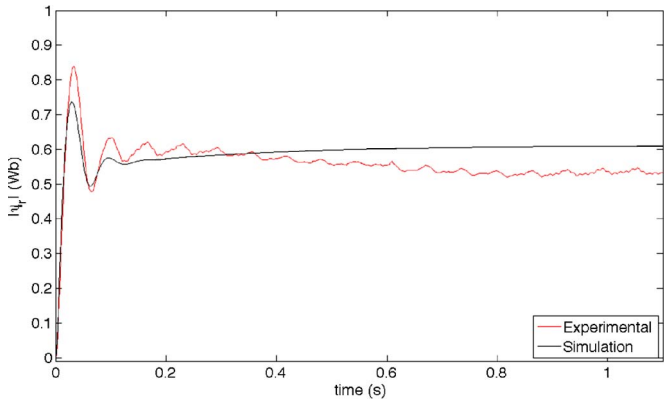

Fig. 28. Induced-part flux linkage for the speed step of 1.8 m/s.

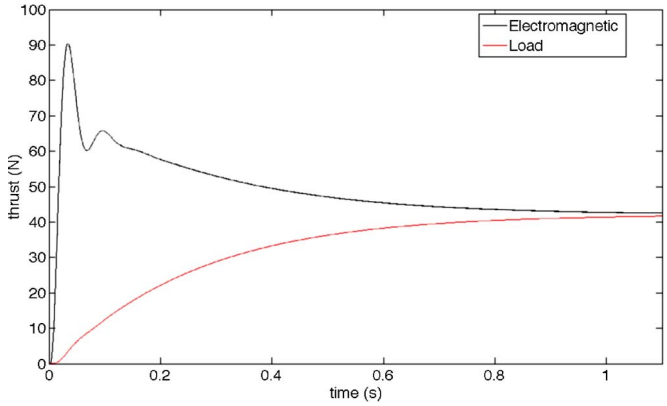

Fig. 29. Thrust and load force for the speed step of 1.8 m/s.

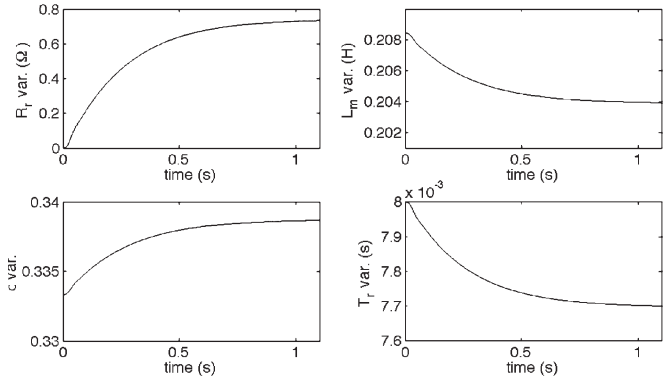

Fig. 30. Modified electrical parameters for the speed step of 1.8 m/s.

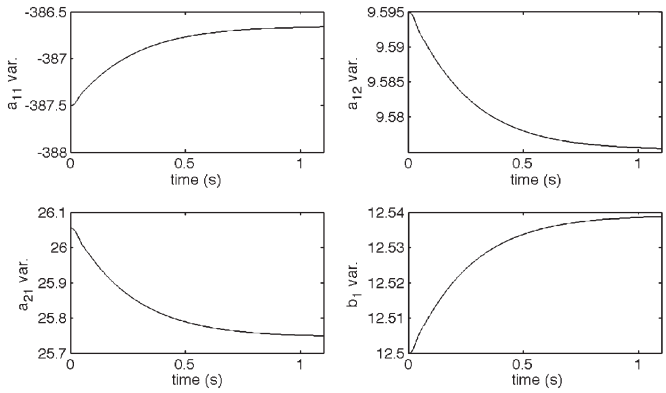

Fig. 31. State model parameters for the speed step of 1.8 m/s.

VIII. Conclusion

This paper has presented the state space-vector model of the LIM taking into consideration the dynamic end effects. Starting from the space-vector equivalent circuit of the LIM, the complete set of space-vector equations has been deduced. Afterward, first the so-called voltage and current flux models have been written, from which the complete state space-vector model has been deduced. The net thrust expression including the end-effect braking force has also been deduced. The complete state space-vector model, electromagnetic and mechanical part, has been implemented in the numerical simulation and has been validated by comparing the results with those obtainable with a FEA and experiments. Results show that, even with a machine with a limited dynamic end effects, the adoption of a this model permits a better estimation of both the electric quantities, e.g., inductor current, and the mechanical quantities, e.g., linear speed, with respect to the classic RIM model.

References

[1] E. R. Laithwaite, "Linear electric machines—A personal view," *Proc. IEEE*, vol. 63, no. 2, pp. 250–290, Feb. 1975.
[2] S. Yamamura, *Theory of the Linear Induction Motor*. Hoboken, NJ, USA: Wiley, 1972.
[3] I. Boldea and S. Nasar, *Linear Electric Motors*. Englewood Cliffs, NJ, USA: Prentice-Hall, 1987.
[4] I. Boldea and S. Nasar, *Linear Motion Electromagnetic Devices*. New York, NY, USA: Taylor & Francis, 2001.
[5] I. Boldea and S. A. Nasar, *Linear Electric Actuators and Generators*. Cambridge, U.K.: Cambridge Univ. Press, 1997.
[6] R. M. Pai, I. Boldea, and S. A. Nasar, "A complete equivalent circuit of a linear induction motor with sheet secondary," *IEEE. Trans. Magn.*, vol. MAG-24, no. 1, pp. 639–654, Jan. 1988.
[7] Duncan and C. Eng, "Linear induction motor-equivalent-circuit model," *Proc. Inst. Elect. Eng.—Elect. Power Appl.*, vol. 130, pt. B, no. 1, pp. 51–57, Jan. 1983.
[8] G. Gentile, N. Rotondale, and M. Scarano, "Analisi del funzionamento transitorio del motore lineare," *L'Energia Elettrica*, no. 5, pp. 205–212, Nov. 1987.
[9] G. Gentile, N. Rotondale, and M. Scarano, "The linear induction motor in transient operation," *L'Energia Elettrica*, no. 7/8, 1988.
[10] V. Isastia, G. Gentile, S. Meo, A. Ometto, N. Rotondale, and M. Scarano, "A voltage feeding algorithm for vectorial control of linear asynchronous machines taking into account end effect," in *Proc. Power Electron. Drives Energy Syst. Ind. Growth*, 1998, vol. 2, pp. 729–734.
[11] J. H. Sung and K. Nam, "A new approach to vector control for a linear induction motor considering end effects," in *Conf. Rec. 34th IEEE IAS Annu. Meeting*, 1999, vol. 4, pp. 2284–2289.
[12] G. Kang and K. Nam, "Field-oriented control scheme for linear induction motor with the end effect," *Proc. Inst. Elect. Eng.—Elect. Power Appl.*, vol. 152, no. 6, pp. 1565–1572, Nov. 2005.

[13] E. F. da Silva, E. Bueno dos Santos, P. C. M. Machado, and M. A. A. de Oliveira, "Dynamic model for linear induction motors," in *Proc. IEEE ICIT*, Maribor, Slovenia, Dec. 2003, pp. 478–482.
[14] H. Kubota, K. Matsuse, and T. Nakano, "DSP-based speed adaptive flux observer of induction motor," *IEEE Trans. Ind. Appl.*, vol. 29, no. 2, pp. 344–348, Mar./Apr. 1993.
[15] M. Cirrincione, M. Pucci, G. Cirrincione, and G. Capolino, "An adaptive speed observer based on a new total least-squares neuron for induction machine drives," *IEEE Trans. Ind. Appl.*, vol. 42, no. 1, pp. 89–104, Jan./Feb. 2006.
[16] A. Accetta, M. Cirrincione, M. Pucci, and G. Vitale, "MRAS speed observer for high performance linear induction motor drives based on linear neural networks," *IEEE Trans. Power Electron.*, vol. 28, no. 1, pp. 123–134, Jan. 2013.
[17] M. Pucci, "Direct field oriented control of linear induction motors," *Elect. Power Syst. Res.*, vol. 89, pp. 11–22, Aug. 2012.
[18] I. Takahashi and Y. Ide, "Decoupling control of thrust and attractive force of a LIM using a space vector control inverter," *IEEE Trans. Ind. Appl.*, vol. 29, no. 1, pp. 161–167, Jan./Feb. 1993.

Marcello Pucci (M'03–SM'11) received the "Laurea" and Ph.D. degrees in electrical engineering from the University of Palermo, Palermo, Italy, in 1997 and 2002, respectively.

In 2000, he was a host student with the Institute of Automatic Control, Technical University of Braunschweig, Brunswick, Germany, working in the field of control of ac machines, with a Grant from the Deutscher Akademischer Austauscdienst—German Academic Exchange Service (DAAD). From 2001 to 2007, he was a Researcher with the Section of Palermo, Institute of Intelligent Systems for Automation (ISSIA–CNR), Palermo, Italy, where he has been a Senior Researcher since 2008. He is a member of the Editorial Board of the *Journal of Electrical Systems*. His current research interests are electrical machines; control, diagnosis, and identification techniques of electrical drives; intelligent control; and power converters.

Dr. Pucci is an Associate Editor of the IEEE TRANSACTIONS ON INDUSTRIAL ELECTRONICS and IEEE TRANSACTIONS ON INDUSTRY APPLICATIONS.